Nano Research 2018, 11(8): 4169–4182
https://doi.org/10.1007/s12274-018-2006-z
Research Article

ISSN 1998-0124
CN 11-5974/O4

Yolk–shell structured Co-C/Void/Co_9S_8 composites with a tunable cavity for ultrabroadband and efficient low-frequency microwave absorption

Xiaofang Liu[1] (✉), Chengcheng Hao[1], Lihua He[2,1], Cheng Yang[2], Yubin Chen[2], Chengbao Jiang[1], and Ronghai Yu[1]

[1] *School of Materials Science and Engineering, Beihang University, Beijing 100191, China*
[2] *Beijing Institute of Aeronautical Materials, Beijing 100095, China*

Received: 4 November 2017
Revised: 3 January 2018
Accepted: 24 January 2018

KEYWORDS

yolk–shell structure,
metal organic framework,
sulfide,
microwave absorption,
broad bandwidth

ABSTRACT

A yolk–shell structured Co-C/Void/Co_9S_8 ternary composite composed of a Co nanoparticle-embedded porous carbon core and Co_9S_8 shell was synthesized by the sulfidation of a Co-based zeolitic imidazolate framework and subsequent pyrolysis. The composition and interior cavity of the Co-C/Void/Co_9S_8 composite could be precisely modulated by controlling the sulfidation reaction. Due to the abundant heterointerfaces, well-controlled cavity, and magnetic–dielectric synergistic effects, the Co-C/Void/Co_9S_8 exhibited excellent and tunable microwave-absorbing properties. The optimized Co-C/Void/Co_9S_8, having a loading of 25 wt.% and thickness only 2.2 mm, displayed an ultrabroad absorption bandwidth of 8.2 GHz at high frequencies. Moreover, the composite could achieve an extremely high reflection loss of –54.02 dB at low frequencies by adjusting its loading to 30 wt.%. This study provides a new insight into promising lightweight microwave-absorbing materials with ultrabroad absorption bandwidths and strong low-frequency absorption.

1 Introduction

The electromagnetic radiation and interference produced by electronic devices and wireless communication have detrimental impacts on device performance, information safety, human health, and the environment [1–4]. Materials capable of eliminating electromagnetic waves therefore attract considerable attention for civil and military applications. Strong microwave absorption can be achieved in traditional magnetic or dielectric absorbers such as ferrites, metallic magnets, and ceramics. Lightweight, thin materials with broad absorption bandwidths are in significant demand for practical applications, and these properties are far beyond the capabilities of traditional absorbers [5, 6]. Among various innovative options, the construction of core–shell and yolk–shell structured absorbers containing dielectric and magnetic com-

---

Address correspondence to liuxf05@buaa.edu.cn

ponents is stimulating considerable interest, because the microwave-absorbing properties can theoretically benefit from the synergistic and interfacial effects between the core and shell [7, 8]. In particular, the yolk–shell structure has the potential to reduce the absorbing layer density due to its unique advantages of large surface areas, low density, and interstitial cavity formation [9–11]. Moreover, the tunable cavity between the yolk and shell is favorable for modulating the effective permittivity and producing multiple reflections within the cavity, providing more opportunities to improve the comprehensive properties. So far, many yolk–shell structured absorbers such as Ni/Void/SnO_2 [12], Fe_3O_4/Void/C [13], Fe_3O_4/Void/ZrO_2 [14], and CoNi/Void/TiO_2 [9] have exhibited strong microwave absorption with reflection losses (RL), exceeding –40 dB in the high frequency region (8–18 GHz). However, it remains a significant challenge for most yolk–shell structured absorbers with low matrix loadings to achieve strong microwave absorptions in a wide frequency-band range. An efficient microwave absorption in the L and S bands (1–4 GHz) is highly desirable because of the wide use of Wi-Fi devices and mobile phones in this frequency range [15]. Generally, strong microwave absorption in L/S bands is achieved with a thick absorbing layer (thickness > 5 mm), which is not appropriate for some practical applications. Thus, the development of a low-frequency absorber with a thin profile is an urgent need for handling electromagnetic interference and pollution.

Recently, Ji's group prepared Co-based zeolitic imidazolate framework (ZIF)/carbonyl iron core–shell composites, and obtained a yolk–shell structured Co-C/Void/carbonyl iron composite by taking advantage of the volume contraction of the ZIF core during pyrolysis [16]. This yolk–shell composite exhibited a strong microwave absorption (RL = −49.2 dB) and broad absorption bandwidth (6.7 GHz) at a relatively low loading of 40 wt.%. This work inspired us to design and fabricate ternary composite absorbers using ZIF as the core. First, the ternary composition can create abundant heterointerfaces in composites, which could enhance microwave absorption by strengthening interfacial polarization. Moreover, the porous core derived from ZIF pyrolysis is favorable for reducing the composite density with respect to the solid cores. Unfortunately, the cavity between the core and the shell which formed by ZIF contraction during pyrolysis could not be tuned over a wide range. In light of the abovementioned advantages of cavities, increasing the volume of the cavity may offer a new opportunity to enhance the microwave-absorbing performance.

In addition, it is well known that the modulation of magnetic and dielectric components to achieve good impedance matching is crucial for improving microwave absorption properties [17, 18]. In prior research on yolk–shell structured absorbers, the magnetic/dielectric component ratio was usually optimized by changing the shell thickness while fixing the core volume, or vice versa. However, the increase of shell or core size may raise the absorber's density. To solve this issue, it is suggested that the amounts of magnetic and dielectric components be changed simultaneously and oppositely. In this way, it is much easier and more effective to improve the impedance matching while reducing the absorber density.

In this work, we used Co-based ZIF as the template to synthesize a yolk–shell structured Co-C/Void/Co_9S_8 (Co-C/Co_9S_8) ternary composite by sulfidation reaction and subsequent pyrolysis (Fig. 1). Co nanoparticles (NPs) were embedded in amorphous carbon, forming the "yolk" of the composite, while Co_9S_8 NPs assembled into a uniform shell that encapsulated the Co-C yolk. By precisely controlling the sulfidation time, the magnetic/dielectric component ratio and the void volume could be modulated simultaneously. Due to the well-designed interior void, the synergistic effect, and the interface effect among ternary components, the Co-C/Co_9S_8 composite with low loading ($\leq$ 30 wt.%) in a paraffin matrix not only exhibited an ultrabroad absorption bandwidth of 8.2 GHz in the X and Ku bands but also achieved a strong microwave absorption (RL = –54.02 dB) in S band.

2 Experimental section

2.1 Materials

Cobalt nitrate hexahydrate ($Co(NO_3)_2 \cdot 6H_2O$, 99%), thioacetamide (TAA), 2-methylimidazole (98%), methanol (99%), and ethanol (99%) were purchased from

Sinapharm Chemical Reagent Co., Ltd. The above reagents were of analytical grade and used without further purification.

2.2 Preparation of ZIF

ZIF polyhedrons were synthesized through a solvothermal reaction. Briefly, 0.984 g of 2-methylimidazole was dissolved in 150 mL of methanol, followed by the addition of 0.873 g of $Co(NO_3)_2{\cdot}6H_2O$. After magnetic stirring for 5 min, the solution was aged at room temperature for 24 h. Then, the purple precipitate was collected by centrifugation, washed with ethanol, and dried under vacuum.

2.3 Preparation of ZIF/sulfide

The ZIF/sulfide core–shell composite was synthesized by an anion-exchange reaction. Under ultrasonication and magnetic stirring, 40 mg of ZIF powder was dispersed in 40 mL of ethanol. Afterwards, 0.18 g of TAA was added to the suspension and maintained at 60 ℃ for 10, 20, 60 and 120 min. The Co:S mole ratio was 1:2.4. The corresponding samples were marked as ZIF/S-2, ZIF/S-3, ZIF/S-4, and ZIF/S-5, respectively. Additionally, 40 mg of ZIF powder was dispersed in 40 mL of ethanol, followed by addition of 90 mg of TAA, and maintained at 60 ℃ for 10 min. The Co/S mole ratio was 1:1.2. The corresponding sample is marked as ZIF/S-1. Finally, the above precipitate was washed with ethanol and dried under vacuum.

2.4 Preparation of Co-C/Co_9S_8

Co-C, Co-C/Co_9S_8 and Co_9S_8-CoS composites were obtained by annealing the as-prepared pure ZIF and ZIF/sulfide powders at 600 ℃ for 2 h under Ar atmosphere with a heating rate of 3 ℃/min. The final products were named Co-C (without sulfidation), Co-C/Co_9S_8-1 (half TAA amount, sulfidation time t_s = 10 min), Co-C/Co_9S_8-2 (t_s = 10 min), Co-C/Co_9S_8-3 (t_s = 20 min), Co-C/Co_9S_8-4 (t_s = 60 min), and Co_9S_8-CoS (t_s = 120 min), respectively. "Co-C" denotes the ZIF-derived composite in which Co NPs were embedded in a carbon matrix. "Co-C/Co_9S_8" represents the yolk (Co-C)–shell (Co_9S_8) structured ternary composites. "Co_9S_8-CoS" marks the hollow binary composite consisting of Co_9S_8 and CoS phases. The overall synthetic process is illustrated in Fig. 1.

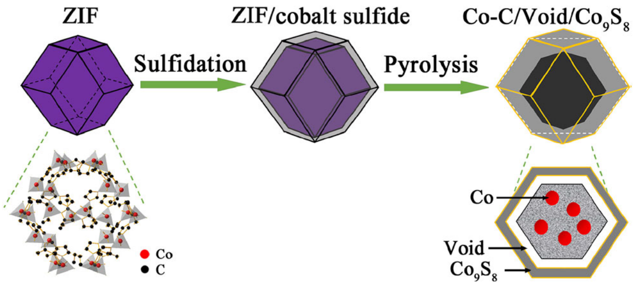

Figure 1 Synthetic processes of the Co-C/Co_9S_8 composite.

2.5 Characterization

The crystal structure of the samples was identified using an X-ray diffractometer (XRD; Rigaku D/MAX–2500). The morphology and microstructure of the samples were investigated by field-emission scanning electron microscopy (FESEM; JEOL–JSM7500) with energy-dispersive X-ray spectroscopy (EDS) equipment and a transmission electron microscope (TEM; JEOL–JEM2100). The composition of the composites was determined by inductively coupled plasma-atomic emission spectroscopy (ICP-AES; ICPS-7500). The specific surface area and pore-size distribution were tested on a QDS-MP-30 volumetric gas sorption instrument. The elemental valence states of the samples were analyzed by X-ray photoelectron spectrometer (XPS; VG ESCALab 220i-XL). Raman spectra were carried out via an in Via Laser Raman spectrometer using a 532 nm laser. The samples used for electromagnetic parameter measurements were prepared by mixing composites with paraffin at different loadings. The mixture was then pressed into a toroidal shape with an outer diameter of 7.00 mm and an inner diameter of 3.04 mm. The complex permittivity and complex permeability were measured by an Agilent N5230C network analyzer in the frequency range of 2–18 GHz.

3 Results and discussion

3.1 Crystal structure

The crystal structures of the intermediate and final products were characterized by XRD. Figure 2(a) shows the XRD patterns of the ZIF before and after sulfidation reaction. The sharp and strong diffraction peaks of pure ZIF reveal its high crystallinity. After a well-controlled reaction with TAA, the diffraction peaks from ZIF weakened as sulfidation time and TAA amount increased, whereas no signals from sulfides could be detected. These findings imply that the crystalline ZIF gradually converted to amorphous sulfides through the reaction between ZIF and sulfur ions released by the decomposition of TAA. When the sulfidation time increased to 2 h, the diffraction peaks were almost invisible in the XRD pattern as a result of the complete conversion to amorphous sulfides.

Figure 2(b) presents the XRD patterns of the samples calcined under Ar atmosphere. The sample calcined from pure ZIF consisted of amorphous carbon and metallic cobalt, while the samples derived from ZIF/sulfide precursors contained different phases. If the sulfidation reaction of the precursor was mild, as is the case for the calcined samples of Co-C/Co_9S_8-1 and Co-C/Co_9S_8-2, the dominant phases were carbon and cobalt together with a small amount of Co_9S_8 with cubic spinel structure (JCPDS no. 190364). As the sulfidation time of the precursors increased, the Co_9S_8 content in the calcined composites gradually increased, while the cobalt and carbon contents decreased and finally disappeared, as observed in the XRD patterns of Co-C/Co_9S_8-3 and Co-C/Co_9S_8-4. When the sulfidation time extended to 120 min, a mixture of Co_9S_8 and CoS (JCPDS no. 750605) phases existed in the calcined sample Co_9S_8-CoS.

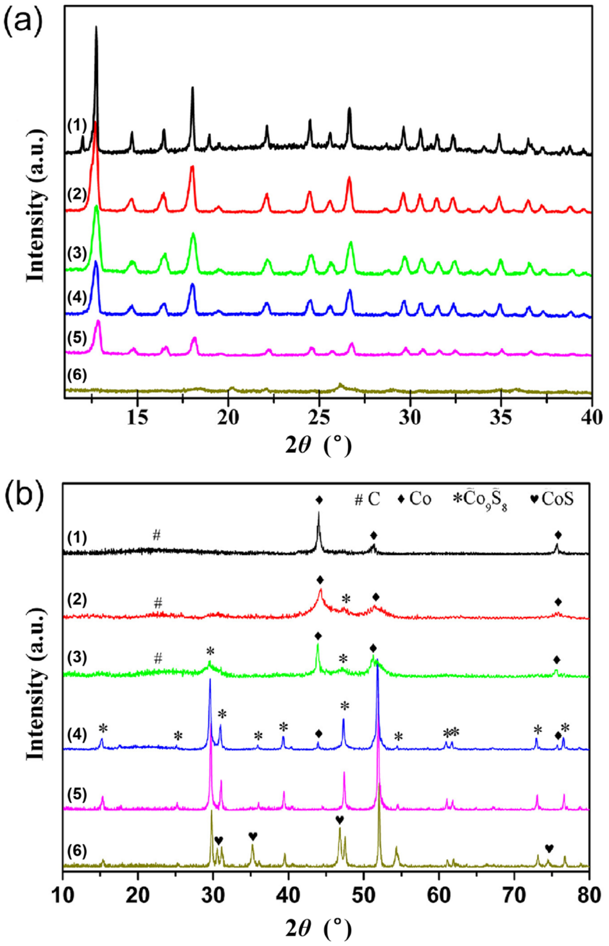

Figure 2 (a) XRD patterns of precursors: curves (1)–(6) correspond to ZIF, ZIF/S-1, ZIF/S-2, ZIF/S-3, ZIF/S-4 and ZIF/S-5, respectively. (b) XRD patterns of the calcined products: curves (1)–(6) correspond to Co-C, Co-C/Co_9S_8-1, Co-C/Co_9S_8-2, Co-C/Co_9S_8-3, Co-C/Co_9S_8-4 and Co_9S_8-CoS, respectively.

3.2 Morphology and microstructure

The morphology and microstructure of the precursors prepared under different sulfidation conditions and their corresponding calcined samples were characterized using SEM and TEM. Figures 3(a) and 3(c) show the SEM and TEM images of pristine ZIF, and display typical rhombic dodecahedra with smooth surfaces. The dodecahedra had a narrow size distribution with a typical edge length of ~ 500 nm. After calcination, the obtained Co-C composite retained the original morphology while its surface became concave and rough (Fig. 3(b)). The reduced Co NPs embedded in the amorphous carbon matrix were uniformly distributed over the entire dodecahedron particle (Fig. 3(d)).

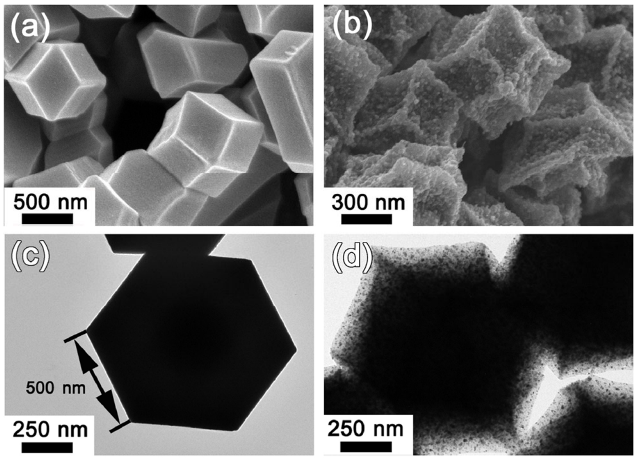

Figure 3 SEM images of (a) pristine ZIF and (b) Co-C composites. TEM images of (c) pristine ZIF and (d) Co-C composites.

Figure 4 presents the SEM images of ZIF/sulfide precursors and the corresponding calcined samples. As observed in Figs. 4(a), 4(c), 4(e), 4(g) and 4(i), after different sulfidation reactions the ZIF/sulfide precursors inherited the morphology of ZIF particles. The particle size did gradually decrease as the sulfidation time increased. When the Co_9S_8 shell was thin, Co NPs derived from the decomposition of residual ZIF core could still be clearly observed on the surface of Co-C/Co_9S_8-1 particles (Fig. 4(b)), although the amount of Co was much lower than that of the Co-C composite (Fig. 3(b)). As the Co_9S_8 shell grew thicker, Co NPs disappeared from the particle surface, as seen in Figs. 4(d), 4(f), 4(h) and 4(j). Detailed information on composition was obtained by ICP-AES measurements, and the results are summarized in Table S1 in the Electronic Supplementary Material (ESM). From Co-C/Co_9S_8-1 to Co-C/Co_9S_8-4, the carbon content decreased from 91.8 at.% to 38.0 at.% while the sulfur content increased from 1.2 at.% to 28.1 at%.

Figure 5 provides the representative TEM images to demonstrate the morphology and microstructure evolutions of the samples with enhanced sulfidation. Various yolk–shell and hollow nanostructures were obtained by precisely tuning the reaction time and TAA amount. Figure 5(a) shows the image of a ZIF/S-1 precursor, which reveals a core–shell structure consisting of a ZIF core and a sulfide shell with a thickness of ~ 25 nm. A narrow gap between the core and shell was formed because the dissolution of ZIF was faster than the deposition of sulfide (Fig. S1(a) in the ESM). The high-magnification TEM image in Fig. 5(b) confirms the amorphous structure of the sulfide shell, which is consistent with the XRD results. After thermal annealing, the obtained Co-C/Co_9S_8-1 sample exhibited a typical yolk–shell structure, as observed in Fig. 5(c). The gap between the Co-C core and Co_9S_8 shell was enlarged compared to that of the precursor due to the volume shrinkage of the core at high temperatures. In contrast to the amorphous

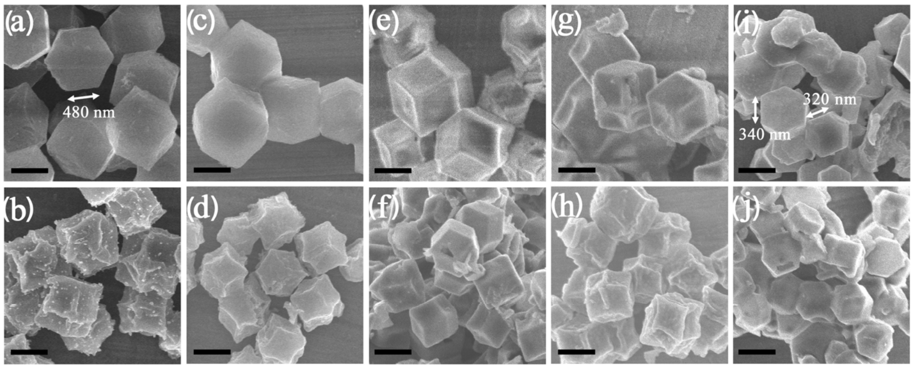

Figure 4 SEM images of (a) ZIF/S-1, (b) Co-C/Co_9S_8-1, (c) ZIF/S-2, (d) Co-C/Co_9S_8-2, (e) ZIF/S-3, (f) Co-C/Co_9S_8-3, (g) ZIF/S-4, (h) Co-C/Co_9S_8-4, (i) ZIF/CoS-5, and (j) Co_9S_8-CoS. The scale bar represents 500 nm.

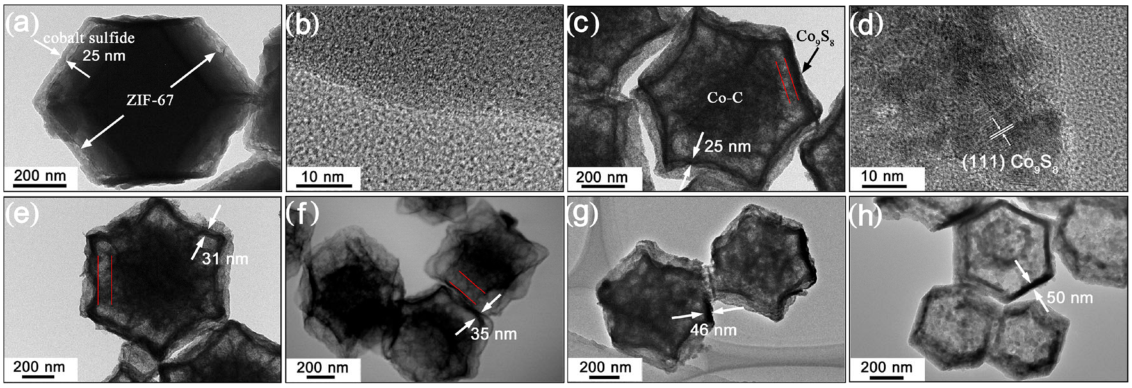

Figure 5 TEM images of (a) ZIF/S-1, (b) amorphous sulfide shell in ZIF/S-1, (c) Co-C/Co_9S_8-1, (d) Co_9S_8 shell in Co-C/Co_9S_8-1, (e) Co-C/Co_9S_8-2, (f) Co-C/Co_9S_8-3, (g) Co-C/Co_9S_8-4, and (h) Co_9S_8-CoS.

shell in ZIF/S-1, the outer shell of Co-C/Co_9S_8-1 was composed of Co_9S_8 NPs with an average size of ~ 5 nm (Fig. 5(d)). As the sulfidation reaction was enhanced, the gap between yolk and shell in the calcined samples became larger (marked by two red lines in images), and simultaneously the curvature of the dodecahedron edge increased (Figs. 5(e)–5(g)). When the sulfidation time was increased to 60 min, the gap in Co-C/Co_9S_8-4 became ambiguous. The representative element mappings of Co-C/Co_9S_8-3 further confirm that the core of the particle is composed of cobalt and carbon, and the shell is cobalt sulfide (Fig. S2 in the ESM). As the sulfidation time reached 120 min, the particles evolved into hollow structures, as shown in Fig. 5(h). The corresponding selected area electron diffraction (SAED) pattern in Fig. S1(b) in the ESM reveals the polycrystalline nature of the composite, and the coexistence of CoS and Co_9S_8 phases.

3.3 Carbon structure and elemental valence state

Detailed structural characterizations of the carbon components in Co-C and Co-C/Co_9S_8 composites were conducted using Raman spectroscopy. As shown in Fig. 6(a), all the Raman spectra displayed peaks at ~ 1,340 and 1,580 cm^{-1}, which are denoted as the D band and G band, respectively. The D band is associated with a disordered carbon or defective graphitic structure, while the G band is a typical feature of graphitic layers [19]. Generally, the graphitization degree of carbon materials can be evaluated by the intensity ratio of the D to G bands (I_D/I_G) [20, 21]. The I_D/I_G values for the samples are approximately 1.09, indicating that the carbon components were highly disordered, and the sulfidation reaction did not change their degree of disorder.

XPS measurements were performed to investigate the elemental valence states of the representative Co-C/Co_9S_8-3 composite. The C 1s spectrum in Fig. 6(b) shows the presence of C–C/C=C (284.7 eV), C–S (285.7 eV), and C=O (288.4 eV) species. Figure 6(c) provides the Co 2p XPS spectrum containing Co $2p_{3/2}$ and satellite peaks. The deconvolution results revealed four peaks belonging to Co^0 at 778.3 eV, Co^{3+} at 781.2 eV, Co^{2+} at 783.2 eV, and a satellite peak at 787.3 eV. The Co^0 species originated from the Co NPs which were embedded in amorphous carbon, while the Co^{3+} and Co^{2+} components arised from the Co_9S_8 and CoS phases [22]. In addition, the S 2p spectrum was fitted with four peaks as presented in Fig. 6(d). The peaks at 161.8 and 163.2 eV could be assigned to S $2p_{3/2}$ and S $2p_{1/2}$ in metal sulfides [23]. The peak at 164.7 eV was attributed to C–S, which indicated that some sulfur atoms bonded to carbon atoms [24, 25]. The strong peak at 168.8 eV was ascribed to oxidized sulfur species (SO_x) produced by the adsorbed oxygen on the Co_9S_8 surface [25, 26].

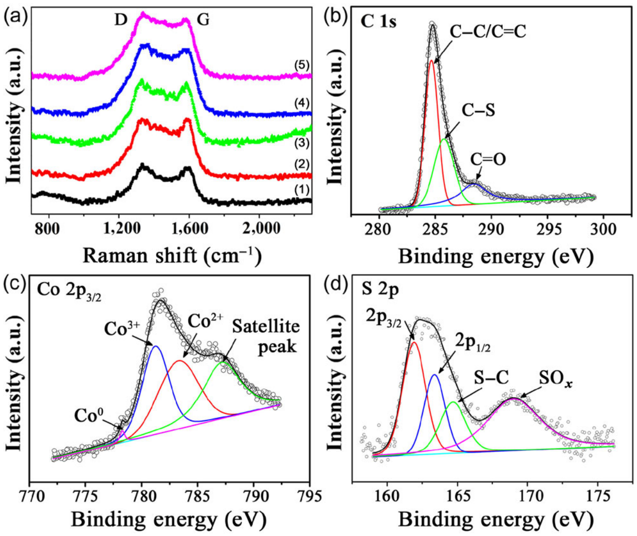

Figure 6 (a) Raman spectra of Co-C and Co-C/Co_9S_8 composites, curve (1)–(5) corresponds to Co-C, Co-C/Co_9S_8-1, Co-C/Co_9S_8-2, Co-C/Co_9S_8-3 and Co-C/Co_9S_8-4, respectively. XPS spectra of Co-C/Co_9S_8-3: (b) C 1s spectrum, (c) Co $2p_{3/2}$ spectrum, and (d) S 2p spectrum.

3.4 Porous characteristics and magnetic properties

The porous character of the representative calcined samples Co-C/Co_9S_8-1, Co-C/Co_9S_8-3, and Co_9S_8-CoS was investigated by nitrogen adsorption–desorption analysis. As shown in Fig. 7, all the measured samples displayed a typical type-IV isotherm with a hysteresis loop in the relative pressure P/P_0 range 0.45–1.0, revealing the mesoporous structure of the composites [27]. As sulfidation time was extended, the Brunauer–Emmett–Teller surface area (S_{BET}) of the composites decreased from ~ 293.0 to ~ 59.3 m^2/g due to the decrease in size of the porous Co-C core and the increase in size of the low-surface-area Co_9S_8 shell, while the pore size remained below 5 nm. Figure S3 in the ESM shows the field-dependent magnetization curves of

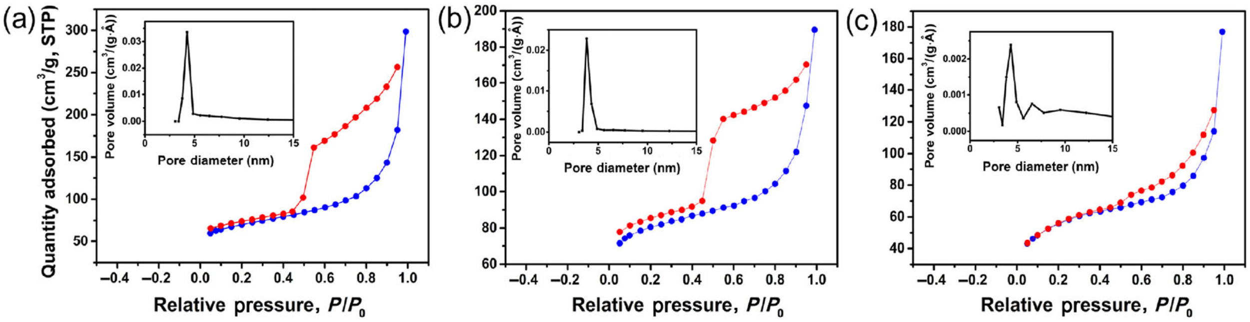

Figure 7 Nitrogen adsorption–desorption isotherms of (a) Co-C/Co_9S_8-1, (b) Co-C/Co_9S_8-3, and (c) Co_9S_8-CoS, inset: corresponding pore-size distribution.

the calcined samples. The presence of metallic Co NPs produced typical ferromagnetic behaviors in the Co-C and Co-C/Co_9S_8 samples. The saturated magnetization (M_s) monotonously decreased from 28.2 to 3.3 emu/g as the Co_9S_8 content increased. In contrast, the Co_9S_8-CoS sample exhibited a paramagnetic state owing to the complete phase conversion from the ferromagnetic cobalt phase to paramagnetic Co_9S_8 and antiferromagnetic CoS phases [28].

3.5 Reflection loss

Transition metal-carbon composites and transition-metal sulfides have been studied extensively for their application as catalysts [25, 29, 30], batteries [31, 32], and supercapacitors [33]. Here, we explored their application in a microwave-absorbing field. To evaluate the microwave-absorbing properties, we selected five representative composites with obvious differences in composition and microstructure for electromagnetic parameter measurements. The as-prepared composites were uniformly dispersed in a paraffin matrix with the same loading of 30 wt.%. The RLs of the samples were calculated using the measured complex permittivity and complex permeability based on the transmission line theory [34, 35]

$$Z_{\mathrm{in}} = Z_0(\mu_{\mathrm{r}}/\varepsilon_{\mathrm{r}})^{1/2}\tanh\left[\mathrm{j}(2\pi f t)(\mu_{\mathrm{r}}\varepsilon_{\mathrm{r}})^{1/2}/c\right] \tag{1}$$

$$\mathrm{RL} = 20\log\left|\frac{Z_{\mathrm{in}} - Z_0}{Z_{\mathrm{in}} + Z_0}\right| \tag{2}$$

where Z_0 and Z_{in} are the characteristic impedance of free space and the input impedance of absorber, respectively, ε_{r} and μ_{r} are the complex permittivity and permeability of the absorber, respectively, f is the frequency of electromagnetic wave, t is the thickness of absorber layer, and c is the velocity of light. Figure 8(a) compares the RL values of the Co-C, Co-C/Co_9S_8-1, Co-C/Co_9S_8-3, Co-C/Co_9S_8-4 and Co_9S_8-CoS samples with layer thicknesses of 1.0–5.0 mm. Relative to Co-C and Co_9S_8-CoS binary composites, the Co-C/Co_9S_8 ternary composites with optimized composition and structure displayed enhanced microwave-absorbing properties with |RL| values above 10 dB, which achieved 90% attenuation of incident microwaves. Among all the samples, the Co-C/Co_9S_8-3 composite exhibited the strongest microwave absorption, and its RL value exceeded –10 dB even at a layer thickness as thin as 1.0 mm. Currently, it is still a challenge to achieve 90% microwave absorption at absorber thicknesses as low as 1.0 mm. Therefore, it is expected that the Co-C/Co_9S_8-3 composite may potentially be applied as an ultrathin absorbing layer.

Furthermore, we systematically investigated the microwave absorbing properties of the Co-C/Co_9S_8-3 composite with different loadings (10 wt.%, 20 wt.%, 25 wt.%, and 30 wt.%). The composites with loadings of 10 wt.% and 20 wt.% did not show effective microwave absorption (|RL| < 10 dB) at 1.0–5.0 mm (Fig. S4 in the ESM). As the loading increased to 25 wt.%, the composite displayed strong microwave absorption in both low- and high-frequency regions (Figs. 8(b) and 8(c)). The gradual shift of the RL peak towards lower frequencies with the increasing layer thickness followed the quarter-wavelength cancellation law [36, 37]. Currently, one of the biggest challenges for microwave absorbing materials is broadening the effective absorption bandwidth (i.e., obtaining

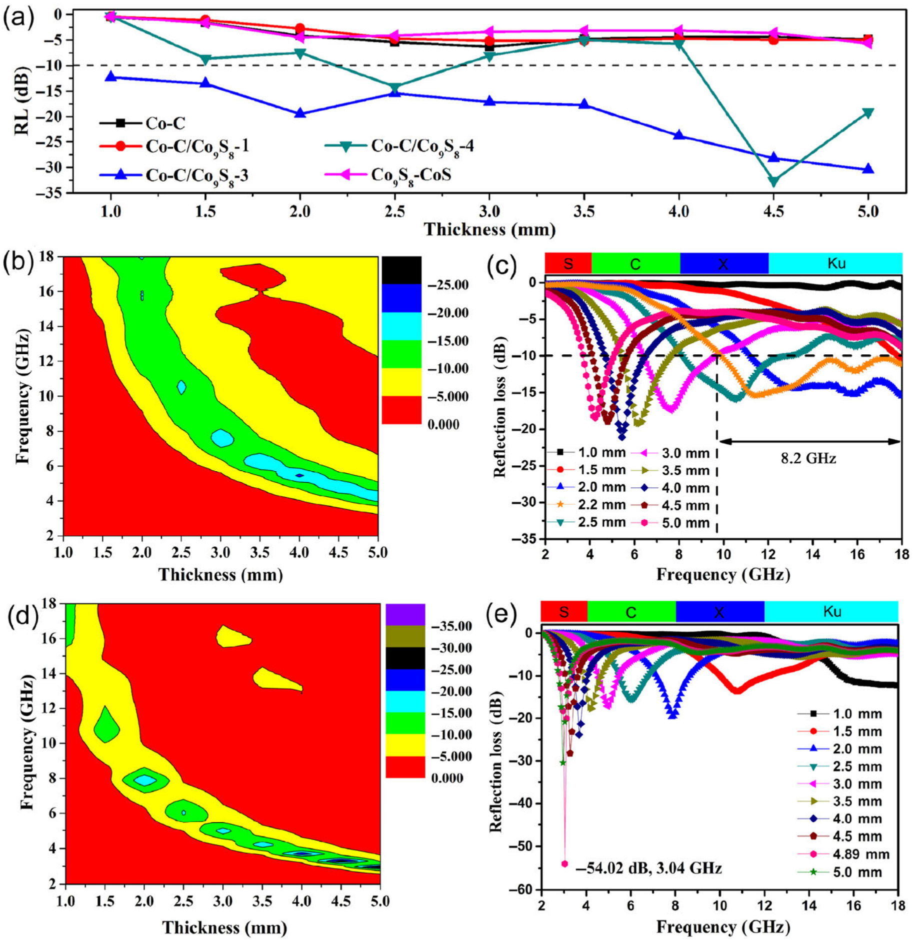

Figure 8 (a) Comparison of RL values of Co-C, Co-C/Co_9S_8-1, Co-C/Co_9S_8-3, Co-C/Co_9S_8-4 and Co_9S_8-CoS samples at a layer thickness of 1.0–5.0 mm (loading of 30 wt.%). Frequency dependences of reflection losses of Co-C/Co_9S_8-3 composites with loadings of ((b) and (c)) 25 wt.% and ((d) and (e)) 30 wt.%.

an absorption bandwidth with RL value lower than –10 dB). Interestingly, the Co-C/Co_9S_8-3 composite with a loading of 25 wt.% possessed an ultrabroad absorption bandwidth up to 8.2 GHz at a layer thickness of 2.2 mm, covering the range of 9.8–18.0 GHz. It is noteworthy that the actual absorption bandwidth of Co-C/Co_9S_8-3 composite could be even wider than 8.2 GHz because the testing frequency ended at 18 GHz.

Additionally, it is attractive to find that the Co-C/Co_9S_8-3 composite achieved strong microwave absorption in S band (2–4 GHz) within a layer thickness of 5.0 mm (Fig. 8(d)). Recently, Tong et al. reported a strong low-frequency microwave absorption of Fe_3O_4/C nanorings [20]. When 60 wt.% of Fe_3O_4/C nanorings were dispersed in paraffin, the sample displayed a minimum RL of –55.68 dB at 3.44 GHz with a layer thickness of 6.2 mm. Herein, the Co-C/Co_9S_8-3 composite showed a comparable microwave absorption in S band with a much lower loading of 30 wt.%. As seen in Fig. 8(e), the minimum RL value was –54.02 dB at 3.04 GHz with a layer thickness of 4.89 mm. Although the Co-C/Co_9S_8-3 composite achieved a strong low-frequency absorption using a thinner layer and a lower loading in comparison with the previous report, further studies are still required to broaden the effective absorption bandwidth to meet the demands of low-frequency applications.

3.6 Microwave absorption mechanism

To understand the mechanisms for the excellent microwave absorbing properties, the complex permittivities and permeabilities of the different composites were analyzed below. Figures 9(a)–9(e) show the real

(ε') and imaginary parts (ε'') of complex permittivities, which represent the storage and loss capabilities of electric energy, respectively [38, 39]. The Co-C/Co_9S_8-3 and Co-C/Co_9S_8-4 ternary composites had larger ε' and ε'' values than those of the others; particularly, the Co-C/Co_9S_8-3 exhibited the largest ε'' values, ranging from 6.8 to 11.6, and strong resonant peaks over the entire frequency range, which implied its strong dielectric-loss capability. Additionally, Fig. S5 in the ESM presents the ε' and ε'' curves of Co-C/Co_9S_8-3 composites with loadings from 10 wt.% to 30 wt.%. Both the ε' and ε'' values monotonously increased as the loading was raised, following the effective-medium theory. Meanwhile, the resonant peaks in the ε'' curves became much stronger. The strong resonant peaks in the ε'' curves of the Co-C/ Co_9S_8-3 and Co-C/Co_9S_8-4 composites suggest enhanced dielectric relaxation behaviors. According to the Debye relaxation theory, the relative complex permittivity (ε_r) can be expressed by the equation [40, 41]

$$\varepsilon_r = \varepsilon' - j\varepsilon'' = \varepsilon_\infty + \frac{\varepsilon_s - \varepsilon_\infty}{1 + j\omega\tau} \tag{3}$$

where τ, ω, ε_s, and ε_∞ are polarization relaxation time, angular frequency, static permittivity and relative permittivity at the high-frequency limit, respectively. It can thus be deduced that

$$\varepsilon' = \varepsilon_\infty + \frac{\varepsilon_s - \varepsilon_\infty}{1 + (\omega\tau)^2} \tag{4}$$

$$\varepsilon'' = \frac{\omega\tau(\varepsilon_s - \varepsilon_\infty)}{1 + (\omega\tau)^2} \tag{5}$$

From Eq. (3), it can be seen that in Eqs. (4) and (5), ε' and ε'' follow the relationship

$$(\varepsilon' - \varepsilon_\infty)^2 + (\varepsilon'') = (\varepsilon_s - \varepsilon_\infty)^2 \tag{6}$$

Therefore, the plot of ε' versus ε'' should be a single semicircle, usually defined as the Cole–Cole semicircle, and each semicircle denotes one Debye relaxation process. As shown in Fig. 9(f), both the ε'–ε'' curves of Co-C/Co_9S_8-3 and Co-C/Co_9S_8-4 composites displayed several overlapped Cole–Cole semicircles, revealing the multiple Debye polarization relaxations. As is well known, the accumulated charges at the heterointerfaces between different dielectric media can produce dipole moments, thus generating Debye-like relaxations under an alternating electromagnetic field [42–44]. Such relaxations could be called interfacial polarization relaxation or Maxwell–Wagner polarization

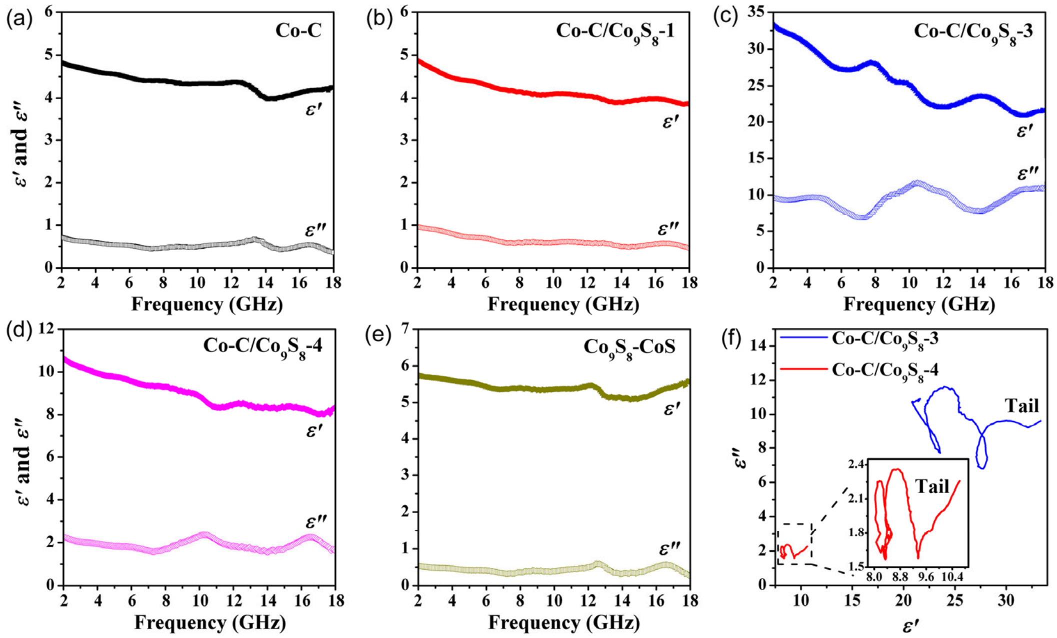

Figure 9 Frequency dependences of ε' and ε'' for (a) Co-C, (b) Co-C/Co_9S_8-1, (c) Co-C/Co_9S_8-3, (d) Co-C/Co_9S_8-4, and (e) Co_9S_8-CoS composites with the same loading of 30 wt.%. (f) Plots of ε'–ε'' of Co-C/Co_9S_8-3 and Co-C/Co_9S_8-4 composites. Inset: the enlarged ε'–ε'' plot of Co-C/Co_9S_8-4.

relaxation. In Co-C, Co-C/Co_9S_8 and Co_9S_8-CoS composites, the accumulation of free charges at Co-C and Co_9S_8-CoS interfaces could produce intense interfacial polarization relaxations. Additionally, the above reported XPS spectra of C and S for the Co-C/Co_9S_8 composite indicated the presence of C–O and S–O bonds due to the adsorption of oxygen from air. Thus, dipoles could form at the void/C and void/Co_9S_8 interfaces because of the different electronegativities of O and C (or S), causing Debye polarization relaxations under an alternating electromagnetic field. Similarly, Debye polarization relaxation also occurred at the C–Co_9S_8 interface in terms of the formation of C–S bond. As sulfidation time increased, the volume of Co-C core gradually decreased and the content of sulfide shell increased. As a result, the interfacial polarizations at the Co/C and C/void interfaces weakened, whereas the Co_9S_8-related interfacial polarizations increased. Thus, the permittivity of the composite could achieve the largest value at the optimum composition, which was just proved to be the Co-C/Co_9S_8-3 composite.

Figure 10 and Fig. S6 in the ESM illustrate the frequency dependence of the permeability of Co-C and Co-C/Co_9S_8 ferromagnetic composites. In the low frequency range, the Co-C composite with the highest saturated magnetization possessed the largest permeability (μ' and μ''), while the formation of the sulfide shell decreased the permeability of Co-C/Co_9S_8. The imaginary part of permeability (μ'') represents the loss capability of magnetic energy. It was found that the μ'' curves showed obvious resonance behaviors with multi-peaks appearing in 2–18 GHz. Generally, the resonant peak at a low frequency is derived from the natural ferromagnetic resonance [45, 46], while the other resonances are assigned to non-uniform exchange resonance modes at a higher frequency [20]. In contrast to the natural resonant frequency (f_r) of bulk Co, which is located the megahertz frequency range, the f_r of the composites shift considerably to higher frequencies due to the enhancement of the anisotropy field H_a according to the equation $2\pi f_r = \gamma H_a$ (γ is the gyromagnetic ratio) [47, 48]. Since H_a is directly proportional to the anisotropy constant, K, ($K = 2\pi M_s H_a$), the increase of H_a could be ascribed to the small size-effect induced increase in K of Co NPs [49]. Based on Chen's study, the K value of Co NPs with a size of 15–50 nm is in the range of $5 \times 10^6 - 30 \times 10^6$ erg/cm^3, much higher than that of bulk Co (2.7×10^6 erg/cm^3) [50]. Therefore, the f_r of Co-C and Co-C/Co_9S_8 composites could shift to gigahertz frequency, which promotes magnetic loss.

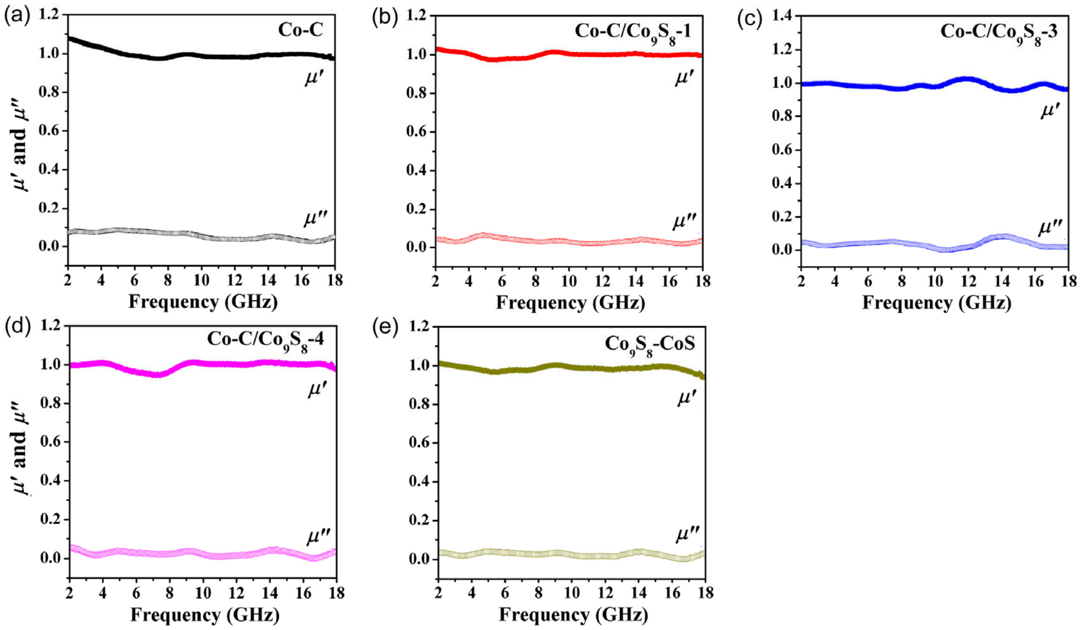

Figure 10 Frequency dependences of μ' and μ'' for (a) Co-C, (b) Co-C/Co_9S_8-1, (c) Co-C/Co_9S_8-3, (d) Co-C/Co_9S_8-4, and (e) Co_9S_8-CoS composites with the same loading of 30 wt.%.

From Figs. 9 and 10, it is seen that the ε'' and μ'' of the Co-C/Co_9S_8 composites do not decay at high frequencies (above 9 GHz), implying that the microwave dissipation capability of the samples is quite stable. Compared with the value of μ'', the larger ε'' value reveals the dominant contribution of dielectric loss to microwave attenuation over the entire frequency range. It is well known that ultimately, microwave dissipation depends on the combined effects of dielectric and magnetic losses [16]. To evaluate the microwave dissipation capability, the attenuation constants (α) of the above samples were calculated as

$$\alpha = \frac{\sqrt{2}\pi f}{c} \times \sqrt{(\mu''\varepsilon'' - \mu'\varepsilon') + \sqrt{(\mu''\varepsilon'' - \mu'\varepsilon')^2 + (\mu'\varepsilon'' + \mu''\varepsilon')^2}} \quad (7)$$

As presented in Fig. S7 in the ESM, the Co-C/Co_9S_8-3 composites with high loadings of 25 wt.% and 30 wt.% possessed large α values, which is an essential reason for strong microwave absorption.

Additionally, it has been widely accepted that the microwave absorbing property of a material does not exclusively depend on the microwave attenuation inside the absorber; impedance matching that determines the reflection of incident microwaves at the air–absorber interface is a necessary precondition for microwave absorption [51, 52]. A detailed study of impedance matching is important for understanding the broad absorption bandwidth at a high frequency for the Co-C/Co_9S_8-3 composite. Ideal impedance matching involves a $|Z_{in}/Z_0|$ value of 1.0, which corresponds to the complete entrance of the incident microwave into the absorber with zero reflection [53]. Figure S8 in the ESM shows the frequency dependencies of RL and $|Z_{in}/Z_0|$ values for Co-C/Co_9S_8-3 composites with loadings of 25 wt.% and 30 wt.%. It is clear that the effective absorption bandwidth is closely related in the impedance matching condition. When the loading of the Co-C/Co_9S_8-3 composite in matrix was 25 wt.%, the $|Z_{in}/Z_0|$ value was close to 1.0 in a wide frequency range; specifically, it fluctuated between 0.7 and 0.9 in the range 10–18 GHz, implying the entrance of incident microwave into the absorber to a large extent [54]. This frequency region coincided with the broad effective absorption bandwidth. According to Ji's report, a moderate ε' value in the range of 10–30 is favorable to the improvement of the impedance-matching behavior [7]. Therefore, the proper ε' of Co-C/Co_9S_8-3 composite (25 wt.%) benefits the impedance matching. The good impedance matching together with the large attenuation constant endows the sample strong microwave absorption in a wide frequency range at high frequency. As to the composite with a loading of 30 wt.%, the good impedance matching only occurred at low frequency in a quite narrow region, thus resulting in the narrow absorption bandwidth.

Based on the above analysis, we can summarize a scheme to illustrate the mechanism of microwave absorption in the Co-C/Co_9S_8 composite. As shown in Fig. 11, the incident microwave first enters the absorber with a good impedance match. Subsequently, the microwave can be dissipated by multiple loss modes including dielectric loss, mainly from multiple interfacial polarization relaxations, as well as magnetic loss from the ferromagnetic and exchange resonances of the Co NPs. Besides, the large cavity between the porous core and sulfide shell could promote microwave dissipation by repeatedly reflecting the incident microwaves, as illustrated in Fig. 11(b) [8, 36]. Meanwhile, the air in the cavity ensures the penetration of most incident microwaves into the porous core with a smaller impedance gap [9, 16].

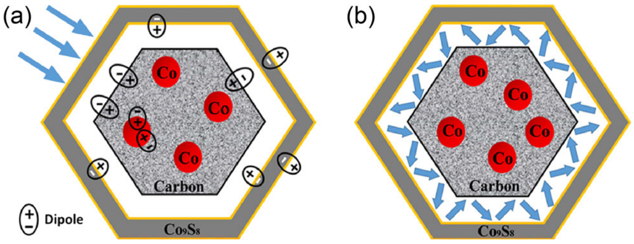

Figure 11 Schematic illustration of the microwave attenuation mechanisms in Co-C/Co_9S_8 composite. (a) Interfacial polarizations in Co-C/Co_9S_8. (b) Microwave reflection in cavity.

4 Conclusions

A Co-C/Co_9S_8 composite with a yolk–shell structure was synthesized using Co-based ZIF as a template, followed by a sulfidation reaction and final annealing. The components and microstructure of the composite could be well tuned by controlling the sulfidation reaction. The optimized light and thin Co-C/Co_9S_8 composite exhibited an ultrabroad absorption bandwidth at a high frequency and an extremely strong microwave absorption at a low frequency. The excellent microwave-absorbing behavior could be ascribed to the large interfacial polarization effect derived from abundant heterointerfaces, the synergistic effect between magnetic and dielectric components, and the tunable cavity between core and shell. This study suggests a new opportunity to develop microwave absorbers with ultrabroad absorption bandwidths and strong low-frequency absorptions.

Acknowledgements

This work was financially supported by the Beijing Municipal Natural Science Foundation (No. 2172031), Beijing Municipal Science and Technology Project (No. Z161100002116029), the Aeronautical Science Foundation of China (No. 2016ZF51049), the National Natural Science Foundation of China (Nos. 51671010 and 51731002), and the Fundamental Research Funds for the Central Universities.

Electronic Supplementary Material: Supplementary material (ICP results, TEM image, SAED pattern, elemental mapping and field-dependent magnetization curves of composites; RL curves of Co/C/Co_9S_8-3 (10 wt.% and 20 wt.%); ε', ε'', μ' and μ'' for Co/C/Co_9S_8-3 with different loadings; attenuation constants of composites; RL curves and relative input impedance for Co/C/Co_9S_8-3 (25 wt.% and 30 wt.%)) is available in the online version of this article at https://doi.org/10.1007/s12274-018-2006-z.

References

[1] Shahzad, F.; Alhabeb, M.; Hatter, C. B.; Anasori, B.; Hong, S. M.; Koo, C. M.; Gogotsi, Y. Electromagnetic interference shielding with 2D transition metal carbides (MXenes). *Science* **2016**, *353*, 1137–1140.

[2] Aissa, B.; Nedil, M.; Kroeger, J.; Hossain, M. I.; Mahmoud, K.; Rosei, F. Nanoelectromagnetic of the N-doped single wall carbon nanotube in the extremely high frequency band. *Nanoscale* **2017**, *9*, 14192–14200.

[3] Ding, Y.; Zhang, Z.; Luo, B. H.; Liao, Q. L.; Liu, S.; Liu, Y. C.; Zhang, Y. Investigation on the broadband electromagnetic wave absorption properties and mechanism of Co_3O_4-nanosheets/reduced-graphene-oxide composite. *Nano Res.* **2017**, *10*, 980–990.

[4] Ding, Y.; Zhang, L.; Liao, Q. L.; Zhang, G. J.; Liu, S.; Zhang, Y. Electromagnetic wave absorption in reduced graphene oxide functionalized with Fe_3O_4/Fe nanorings. *Nano Res.* **2016**, *9*, 2018–2025.

[5] Liu, X. F.; Cui, X. R.; Chen, Y. X.; Zhang, X. J.; Yu, R. H.; Wang, G. S.; Ma, H. Modulation of electromagnetic wave absorption by carbon shell thickness in carbon encapsulated magnetite nanospindles-poly(vinylidene fluoride) composites. *Carbon* **2015**, *95*, 870–878.

[6] Jiang, W. C.; Wu, F.; Jiang, Y. J.; Sun, M. X.; Zhang, K.; Xia, Y. L.; Wang, D. R.; Xie, A. M. Synthesis of hollow $Cu_{1.8}S$ nano-cubes for electromagnetic interference shielding. *Nanoscale* **2017**, *9*, 10961–10965.

[7] Lv, H. L.; Guo, Y. H.; Wu, G. L.; Ji, G. B.; Zhao, Y.; Xu, Z. J. Interface polarization strategy to solve electromagnetic wave interference issue. *ACS Appl. Mater. Interfaces* **2017**, *9*, 5660–5668.

[8] Feng, J. T.; Hou, Y. H.; Wang, Y. C.; Li, L. C. Synthesis of hierarchical $ZnFe_2O_4$@SiO_2@RGO core–shell microspheres for enhanced electromagnetic wave absorption. *ACS Appl. Mater. Interfaces* **2017**, *9*, 14103–14111.

[9] Liu, Q. H.; Cao, Q.; Bi, H.; Liang, C. Y.; Yuan, K. P.; She, W.; Yang, Y. J.; Che, R. C. CoNi@SiO_2@TiO_2 and CoNi@Air@TiO_2 microspheres with strong wideband microwave absorption. *Adv. Mater.* **2016**, *28*, 486–490.

[10] You, W. B.; Bi, H.; She, W.; Zhang, Y.; Che, R. C. Dipolar-distribution cavity gamma-Fe_2O_3@C@alpha-MnO_2 nanospindle with broadened microwave absorption bandwidth by chemically etching. *Small* **2017**, *13*, 1602779.

[11] Zhang, X. M.; Ji, G. B.; Liu, W.; Quan, B.; Liang, X. H.; Shang, C. M.; Cheng, Y.; Du, Y. W. Thermal conversion of an Fe_3O_4@metal-organic framework: A new method for an efficient Fe-Co/nanoporous carbon microwave absorbing material. *Nanoscale* **2015**, *7*, 12932–12942.

[12] Zhao, B.; Guo, X. Q.; Zhao, W. Y.; Deng, J. S.; Fan, B. B.; Shao, G.; Bai, Z. Y.; Zhang, R. Facile synthesis of yolk–shell Ni@void@SnO_2(Ni_3Sn_2) ternary composites via galvanic replacement/Kirkendall effect and their enhanced microwave absorption properties. *Nano Res.* **2017**, *10*, 331–343.

[13] Tian, C. H.; Du, Y. C.; Cui, C. S.; Deng, Z. L.; Xue, J. L.; Xu, P.; Qiang, R.; Wang, Y.; Han, X. J. Synthesis and microwave absorption enhancement of yolk–shell Fe_3O_4@C microspheres. *J. Mater. Sci.* **2017**, *52*, 6349–6361.

[14] Yu, M.; Liang, C. Y.; Liu, M. M.; Liu, X. L.; Yuan, K. P.;

Cao, H.; Che, R. C. Yolk–shell Fe_3O_4@ZrO_2 prepared by a tunable polymer surfactant assisted sol-gel method for high temperature stable microwave absorption. *J. Mater. Chem. C* **2014**, *2*, 7275–7283.

[15] Hou, Y.; Cheng, L. F.; Zhang, Y. N.; Yang, Y.; Deng, C. R.; Yang, Z. H.; Chen, Q.; Wang, P.; Zheng, L. X. Electrospinning of Fe/SiC hybrid fibers for highly efficient microwave absorption. *ACS Appl. Mater. Interfaces* **2017**, *9*, 7265–7271.

[16] Quan, B.; Liang, X. H.; Ji, G. B.; Ma, J. N.; Ouyang, P. Y.; Gong, H.; Xu, G. Y.; Du, Y. W. Strong electromagnetic wave response derived from the construction of dielectric/magnetic media heterostructure and multiple interfaces. *ACS Appl. Mater. Interfaces* **2017**, *9*, 9964–9974.

[17] Sun, D. P.; Zou, Q.; Qian, G. Q.; Sun, C.; Jiang, W.; Li, F. S. Controlled synthesis of porous Fe_3O_4-decorated graphene with extraordinary electromagnetic wave absorption properties. *Acta Mater.* **2013**, *61*, 5829–5834.

[18] Yin, Y. C.; Liu, X. F.; Wei, X. J.; Yu, R. H.; Shui, J. L. Porous CNTs/Co composite derived from zeolitic imidazolate framework: A lightweight, ultrathin, and highly efficient electromagnetic wave absorber. *ACS Appl. Mater. Interfaces* **2016**, *8*, 34686–34698.

[19] Mohr, M.; Daccache, L.; Horvat, S.; Brühne, K.; Jacob, T.; Fecht, H. J. Influence of grain boundaries on elasticity and thermal conductivity of nanocrystalline diamond films. *Acta Mater.* **2017**, *122*, 92–98.

[20] Wu, T.; Liu, Y.; Zeng, X.; Cui, T. T.; Zhao, Y. T.; Li, Y.; Tong, G. X. Facile hydrothermal synthesis of Fe_3O_4/C core–shell nanorings for efficient low-frequency microwave absorption. *ACS Appl. Mater. Interfaces* **2016**, *8*, 7370–7380.

[21] Chuai, D.; Liu, X. F.; Yu, R. H.; Ye, J. R.; Shi, Y. Q. Enhanced microwave absorption properties of flake-shaped FePCB metallic glass/graphene composites. *Compos. Part A* **2016**, *89*, 33–39.

[22] Zeng, P. Y.; Li, J. W.; Ye, M.; Zhuo, K. F.; Fang, Z. *In situ* formation of Co_9S_8/N-C hollow nanospheres by pyrolysis and sulfurization of ZIF-67 for high-performance lithium-ion batteries. *Chem.—Eur. J.* **2017**, *23*, 9438.

[23] Long, J. Y.; Gong, Y.; Lin, J. H. Metal-organic framework-derived Co_9S_8@CoS@CoO@C nanoparticles as efficient electro- and photo-catalysts for the oxygen evolution reaction. *J. Mater. Chem. A* **2017**, *5*, 10495–10509.

[24] Cao, X. C.; Zheng, X. J.; Tian, J. H.; Jin, C.; Ke, K.; Yang, R. Z. Cobalt sulfide embedded in porous nitrogen-doped carbon as a bifunctional electrocatalyst for oxygen reduction and evolution reactions. *Electrochim. Acta* **2016**, *191*, 776–783.

[25] Alshehri, S. M.; Ahmed, J.; Khan, A.; Naushad, M.; Ahamad, T. Bifunctional electrocatalysts (Co_9S_8@NSC) derived from a polymer-metal complex for the oxygen reduction and oxygen evolution reactions. *ChemElectroChem* **2018**, *5*, 355–361.

[26] Tang, X. K.; Huang, J.; Feng, Q. M.; Liu, K.; Luo, X. P.; Li, Z. S. Carbon sphere@Co_9S_8 yolk–shell structure with good morphology stability for improved lithium storage performance. *Nanotechnology* **2017**, *28*, 375402.

[27] Liu, X. F.; Cui, X. R.; Liu, Y. D.; Yin, Y. D. Stabilization of ultrafine metal nanocatalysts on thin carbon sheets. *Nanoscale* **2015**, *7*, 18320–18326.

[28] Lei, M.; Fu, X. L.; Yang, H. J.; Wang, Y. G.; Zhang, Y. B.; Li, P. G. Solvothermal route to S-deficient CoS nanoplates and their cathodoluminescence and magnetic properties. *J. Nanosci. Nanotechnol.* **2012**, *12*, 2586–2590.

[29] Zeng, X.; Shui, J.; Liu, X.; Liu, Q.; Li, Y.; Shang, J.; Zheng, L.; Yu, R. Single-atom to single-atom grafting of Pt_1 onto Fe-N_4 center: Pt_1@Fe-N-C multifunctional electrocatalyst with significantly enhanced properties. *Adv. Energy Mater.* **2018**, *8*, 1701345.

[30] Liu, Q. T.; Liu, X. F.; Zheng, L. R.; Shui, J. L. The solid-phase synthesis of an Fe-N-C electrocatalyst for high-power proton-exchange membrane fuel cells. *Angew. Chem., Int. Ed.* **2018**, *57*, 1204–1208.

[31] Geng, H. B.; Yang, J.; Dai, Z. F.; Zhang, Y.; Zheng, Y.; Yu, H.; Wang, H. W.; Luo, Z. Z.; Guo, Y. Y.; Zhang, Y. F. et al. Co_9S_8/MoS_2 yolk–shell spheres for advanced Li/Na storage. *Small* **2017**, *13*, 1603490.

[32] Fan, H. H.; Li, H. H.; Huang, K. C.; Fan, C. Y.; Zhang, X. Y.; Wu, X. L.; Zhang, J. P. Metastable marcasite-FeS_2 as a new anode material for lithium ion batteries: CNFs-improved lithiation/delithiation reversibility and Li-storage properties. *ACS Appl. Mater. Interfaces* **2017**, *9*, 10708–10716.

[33] Lu, F.; Zhou, M.; Li, W. R.; Weng, Q. H.; Li, C. L.; Xue, Y. M.; Jiang, X. F.; Zeng, X. H.; Bando, Y.; Golberg, D. Engineering sulfur vacancies and impurities in $NiCo_2S_4$ nanostructures toward optimal supercapacitive performance. *Nano Energy* **2016**, *26*, 313–323.

[34] Zhao, H. B.; Fu, Z. B.; Chen, H. B.; Zhong, M. L.; Wang, C. Y. Excellent electromagnetic absorption capability of Ni/carbon based conductive and magnetic foams synthesized via a green one pot route. *ACS Appl. Mater. Interfaces* **2016**, *8*, 1468–1477.

[35] Lv, H. L.; Liang, X. H.; Ji, G. B.; Zhang, H. Q.; Du, Y. W. Porous three-dimensional flower-like Co/CoO and its excellent electromagnetic absorption properties. *ACS Appl. Mater. Interfaces* **2015**, *7*, 9776–9783.

[36] Yang, Z. H.; Lv, H. L.; Wu, R. B. Rational construction of graphene oxide with MOF-derived porous NiFe@C nanocubes for high-performance microwave attenuation. *Nano Res.*

2016, *9*, 3671–3682.

[37] Lv, H. L.; Zhang, H. Q.; Ji, G. B.; Xu, Z. J. Interface strategy to achieve tunable high frequency attenuation. *ACS Appl. Mater. Interfaces* **2016**, *8*, 6529–6538.

[38] Tian, X.; Meng, F. B.; Meng, F. C.; Chen, X. N.; Guo, Y. F.; Wang, Y.; Zhu, W. J.; Zhou, Z. W. Synergistic enhancement of microwave absorption using hybridized polyaniline@helical CNTs with dual chirality. *ACS Appl. Mater. Interfaces* **2017**, *9*, 15711–15718.

[39] Zhang, X. M.; Ji, G. B.; Liu, W.; Zhang, X. X.; Gao, Q. W.; Li, Y. C.; Du, Y. W. A novel Co/TiO_2 nanocomposite derived from a metal-organic framework: Synthesis and efficient microwave absorption. *J. Mater. Chem. C* **2016**, *4*, 1860–1870.

[40] Yan, L. L.; Liu, J.; Zhao, S. C.; Zhang, B.; Gao, Z.; Ge, H. B.; Chen, Y.; Cao, M. S.; Qin, Y. Coaxial multi-interface hollow Ni-Al_2O_3-ZnO nanowires tailored by atomic layer deposition for selective-frequency absorptions. *Nano Res.* **2017**, *10*, 1595–1607.

[41] Liu, X. F.; Nie, X. Y.; Yu, R. H.; Feng, H. B. Design of dual-frequency electromagnetic wave absorption by interface modulation strategy. *Chem. Eng. J.* **2018**, *334*, 153–161.

[42] She, W.; Bi, H.; Wen, Z. W.; Liu, Q. H.; Zhao, X. B.; Zhang, J.; Che, R. C. Tunable microwave absorption frequency by aspect ratio of hollow polydopamine@α-MnO_2 microspindles studied by electron holography. *ACS Appl. Mater. Interfaces* **2016**, *8*, 9782–9789.

[43] Chen, N.; Jiang, J. T.; Xu, C. Y.; Yuan, Y.; Gong, Y. X.; Zhen, L. Co_7Fe_3 and Co_7Fe_3@SiO_2 nanospheres with tunable diameters for high-performance electromagnetic wave absorption. *ACS Appl. Mater. Interfaces* **2017**, *9*, 21933–21941.

[44] Lv, H. L.; Ji, G. B.; Liang, X. H.; Zhang, H. Q.; Du, Y. W. A novel rod-like MnO_2@Fe loading on graphene giving excellent electromagnetic absorption properties. *J. Mater. Chem. C* **2015**, *3*, 5056–5064.

[45] Liu, X. F.; Chen, Y. X.; Cui, X. R.; Zeng, M.; Yu, R. H.; Wang, G. S. Flexible nanocomposites with enhanced microwave absorption properties based on Fe_3O_4/SiO_2 nanorods and polyvinylidene fluoride. *J. Mater. Chem. A* **2015**, *3*, 12197–12204.

[46] Yang, Y.; Li, M.; Wu, Y. P.; Wang, T.; Choo, E. S. G.; Ding, J.; Zong, B. Y.; Yang, Z. H.; Xue, J. M. Nanoscaled self-alignment of Fe_3O_4 nanodiscs in ultrathin rGO films with engineered conductivity for electromagnetic interference shielding. *Nanoscale* **2016**, *8*, 15989–15998.

[47] Ren, X.; Yang, H. T.; Tang, J.; Li, Z. A.; Su, Y. K.; Geng, S.; Zhou, J.; Zhang, X. Q.; Cheng, Z. H. An effective way to increase the high-frequency permeability of Fe_3O_4 nanorods. *Nanoscale* **2016**, *8*, 12910–12916.

[48] Liu, Q. T.; Liu, X. F.; Feng, H. B.; Shui, H. C.; Yu, R. H. Metal organic framework-derived Fe/carbon porous composite with low Fe content for lightweight and highly efficient electromagnetic wave absorber. *Chem. Eng. J.* **2017**, *314*, 320–327.

[49] Yin, Y. C.; Liu, X. F.; Wei, X. J.; Li, Y.; Nie, X. Y.; Yu, R. H.; Shui, J. L. Magnetically aligned Co-C/MWCNTs composite derived from MWCNT-interconnected zeolitic imidazolate frameworks for a lightweight and highly efficient electromagnetic wave absorber. *ACS Appl. Mater. Interfaces* **2017**, *9*, 30850–30861.

[50] Chen, J. P.; Sorensen, C. M.; Klabunde, K. J.; Hadjipanayis, G. C. Magnetic properties of nanophase cobalt particles synthesized in inversed micelles. *J. Appl. Phys.* **1994**, *76*, 6316–6318.

[51] Liu, X. F.; Hao, C. C.; Jiang, H.; Zeng, M.; Yu, R. H. Hierarchical $NiCo_2O_4$/Co_3O_4/NiO porous composite: A lightweight electromagnetic wave absorber with tunable absorbing performance. *J. Mater. Chem. C* **2017**, *5*, 3770–3778.

[52] Lv, H. L.; Zhang, H. Q.; Zhao, J.; Ji, G. B.; Du, Y. W. Achieving excellent bandwidth absorption by a mirror growth process of magnetic porous polyhedron structures. *Nano Res.* **2016**, *9*, 1813–1822.

[53] Gholipur, R.; Khorshidi, Z.; Bahari, A. Enhanced absorption performance of carbon nanostructure based metamaterials and tuning impedance matching behavior by an external AC electric field. *ACS Appl. Mater. Interfaces* **2017**, *9*, 12528–12539.

[54] González, M.; Crespo, M.; Baselga, J.; Pozuelo, J. Carbon nanotube scaffolds with controlled porosity as electromagnetic absorbing materials in the gigahertz range. *Nanoscale* **2016**, *8*, 10724–10730.